J Solid State Electrochem (2006) 10: 663–673
DOI 10.1007/s10008-006-0141-z

ORIGINAL PAPER

V. V. Kharton · A. V. Kovalevsky · A. A. Yaremchenko · F. M. M. Snijkers · J. F. C. Cooymans · J. J. Luyten · A. A. Markov · J. R. Frade · F. M. B. Marques

Oxygen transport and thermomechanical properties of $SrFe(Al)O_{3-\delta}-SrAl_2O_4$ composites: microstructural effects

Received: 5 December 2005 / Accepted: 30 January 2006 / Published online: 13 April 2006

Abstract Measurements of oxygen permeation through dense $Sr_{1-x}(Fe,Al)O_{3-\delta} - SrAl_2O_4$ composite membranes showed a considerable influence of processing conditions on the surface exchange kinetics, while the bulk ambipolar conductivity is almost unaffected by microstructural factors. Compared to the materials prepared via the glycine–nitrate process (GNP), the surface limitations to oxygen transport are significantly higher for dual-phase $(SrFe)_{0.7}(SrAl_2)_{0.3}O_{3.3-\delta}$ made of a commercial powder synthesized by spray pyrolysis. This difference in behavior may be related to compositional inhomogeneities in the grains of A-site deficient perovskite phase and an enhanced surface concentration of grain boundaries in the case of GNP-synthesized composite, which has also smaller grain size, slightly higher thermal expansion and lower total conductivity. No essential effects on Vickers hardness, varying in the range 6.3–6.5 GPa, were found. The deposition of porous catalyst layers onto the composite surface exposed to reducing environment leads to membrane decomposition. For the fabrication of tubular membranes, the cold isostatic pressing technique was, hence, combined with mechanical treatment to increase the specific surface area without incorporation of catalytically active components.

Keywords Oxide composite · Mixed-conducting membrane · Ferrite · Ceramic microstructure · Oxygen permeability

V. V. Kharton (✉) · A. V. Kovalevsky · A. A. Yaremchenko · J. R. Frade · F. M. B. Marques
Department of Ceramics and Glass Engineering, CICECO, University of Aveiro, 3810-193 Aveiro, Portugal
e-mail: kharton@cv.ua.pt
Tel.: +351-234-370263
Fax: +351-234-425300

V. V. Kharton
Institute of Physicochemical Problems, Belarus State University, 14 Leningradskaya Str., 220050 Minsk, Belarus

F. M. M. Snijkers · J. F. C. Cooymans · J. J. Luyten
Materials Department, Flemish Institute for Technological Research (VITO), 2400 Mol, Belgium

A. A. Markov
Ural Division of RAS, Institute of Solid State Chemistry, 91 Pervomayskaya Str., Ekaterinburg, 620219, Russia

Introduction

Mixed-conducting ceramic membranes attract a significant attention due to their potential application for the separation of high-purity oxygen from air and partial oxidation of light hydrocarbons [1–5]. The key advantage of these membrane systems is the possibility to integrate oxygen separation and catalytic oxidation into a single step, thus providing considerable savings in energy and capital compared to the conventional syngas production method by steam reforming of methane. However, in terms of commercial feasibility, the requirements to mixed-conducting materials include often incompatible targets of high-oxygen permeability and chemical and mechanical stability under severe operating conditions. One promising group of mixed conductors comprises perovskite-related materials derived from $SrFeO_{3-\delta}$ with relatively high oxygen permeability and thermodynamic stability [4–7]. At the same time, the ferrite-based materials exhibiting maximum ionic transport possess serious disadvantages, including insufficient mechanical strength and large thermal and chemically induced expansion. A suitable approach to enhance the dimensional stability is the incorporation of cations having a stable oxidation state, such as Al^{3+} [6, 7]. While the solid solution formation range in $SrFe_{1-y}Al_yO_{3-\delta}$ system corresponds to y=0–0.35, overstoichiometric additions of alumina lead to the segregation of $SrAl_2O_4$ phase, simultaneously improving sintering and increasing oxygen permeation [6]. Similar tendencies were identified for

$(SrFe)_{1-x}(SrAl_2)_xO_{3+x-\delta}$ composites, where moderate amounts of $SrAl_2O_4$ increase thermal shock stability and hardness without detrimental influence on the transport properties [8]. The solubility of iron in the monoclinic $SrAl_2O_4$ lattice is lower than 5% [8]. As illustrated by Fig. 1, an optimum combination of mechanical and oxygen permeability is characteristic of composites with moderate strontium aluminate content, such as $(SrFe)_{0.7}(SrAl_2)_{0.3}O_{3.3-\delta}$ [8].

The present work was focused on the assessment of relationships between the synthesis method, microstructure and oxygen transport in these composite materials. As the preparation procedure may significantly affect both ambipolar conductivity and oxygen surface exchange [9–14], the development of ceramic membranes requires knowledge, mainly empirical, on the role of processing route. Theoretical prediction and even unambiguous interpretation of observed phenomena are often difficult due to the complex nature of transport processes at the grain boundaries and on the surface of ceramics. The oxygen ionic conductivity of single-phase materials, prepared by a similar method with monotonous variation of the processing conditions, typically increases with increasing grain size when the total interfacial resistance decreases [9, 10].

On the other hand, the opposite trends are also well-known, particularly due to high content of mobile defects near the grain boundaries, local ordering processes, and/or dopant segregation [11–13]. The same factors should influence the surface exchange kinetics, which exhibits an even more complicated dependence on the concentration of catalytically active centers and extended defects, ion diffusivity in the oxide surface layers, and local inhomogeneities, such as impurity separation on the surface [9–16]. For example, the partial ionic and electronic conductivities of $LaGa_{0.65}Ni_{0.20}Mg_{0.15}O_{3-\delta}$ membranes prepared by the standard ceramic route and glycine–nitrate process (GNP), were found essentially independent of the synthesis method due to a moderate difference in the ceramic microstructures; however, the surface exchange limitations to oxygen permeation are considerably higher in the former case [14]. An inverse situation was reported for $La_{0.5}Sr_{0.5}FeO_{3-\delta}$ ceramics [13], where changing grain size has no effect on the exchange rate, but influences ionic conduction. To assess microstructural factors determining oxygen transport through $Sr_{1-x}(Fe,Al)O_{3-\delta} - SrAl_2O_4$ composites, relative contributions of the surface exchange and bulk ambi-polar conductivity were evaluated, studying the membrane thickness dependencies of oxygen permeability for the composite ceramics prepared by two different methods.

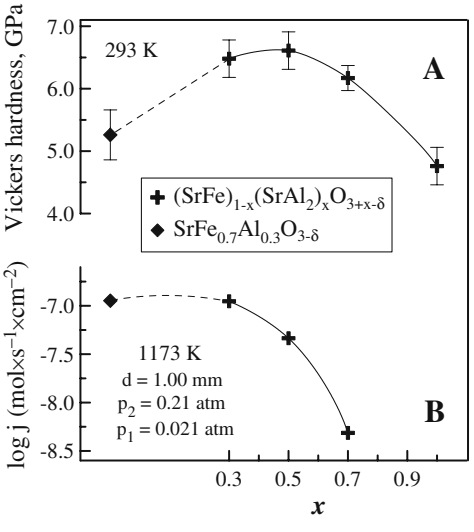

Fig. 1 Relationship between Vickers hardness (**a**) and oxygen permeation fluxes (**b**) through $Sr_{1-x}(Fe, Al)O_{3-\delta} - SrAl_2O_4$ composite membranes synthesized by GNP

Experimental

Submicron powders of $(SrFe)_{0.7}(SrAl_2)_{0.3}O_{3.3-\delta}$ and $(Sr_{0.95}Fe_{0.8}Al_{0.2})_{0.85}(SrAl_2)O_{3.02-\delta}$ were initially prepared by the glycine–nitrate process (GNP), a self-combustion method using glycine as fuel and nitrates of the metal components as oxidant [17]. In the course of synthesis, glycine was added in an aqueous nitrate solution containing metal cations in the stoichiometric proportion; the glycine/nitrate molar ratio was 1.5–2.0 of the stoichiometric one. The solutions were then heated on a hot plate until self-combustion. The resultant powders having a foamed structure were annealed at 1173 K for 2 h to remove residual organic substances, and then ball-milled. Gas-tight ceramic disks were pressed at 250–350 MPa and sintered at 1623 K in air for 5 h. This processing route is hereafter referred to as method 1. As an alternative, commercial $(SrFe)_{0.7}(SrAl_2)_{0.3}O_{3.3-\delta}$ powder (Praxair Surface Technologies, Seattle, WA, USA) synthesized by the combustion spray pyrolysis technique was annealed at 1250–1270 K, milled, compacted at 180–300 MPa and sintered under similar conditions, namely at 1623 K during 5 h in atmospheric air. This procedure is identified as method 2.

After sintering and polishing with diamond pastes, all materials were annealed in air at 1170–1270 K for 2–3 h and slowly furnace-cooled to achieve equilibrium with atmospheric oxygen at low temperatures. Table 1 lists the values of ceramics density (ρ_{exp}). The overall cation composition of as-prepared composites was verified by inductively coupled plasma (ICP) spectroscopic analysis. The materials were characterized by X-ray diffraction (XRD) analysis, scanning electron microscopy combined with energy dispersive spectroscopy (SEM/EDS), dilatometry, and measurements of the total conductivity (4-probe DC) and steady-state oxygen permeability. Vickers hardness tests were performed using one Eseway tester under the load of 10 kg (98.07 N) applied for 15 s. Thermal expansion of ceramic samples was measured using an alumina Linseis L75V/1250 dilatometer with a constant heating rate of 3 K/min in air. The experimental procedures and equipment used for the characterization were reported elsewhere ([6–15] and references cited). All data on the

Table 1 Properties of composite ceramics

Composition	Preparation technique	ρ_{exp}, g/cm^3	Average TEC $\bar{\alpha} \times 10^6$, K^{-1}	Vickers hardness, GPa
$(SrFe)_{0.7}(SrAl_2)_{0.3}O_{3.3-\delta}$	Method 1	4.50	12.73±0.03 (350–920 K) 25.22±0.08 (950–1230 K)	6.5±0.3
$(SrFe)_{0.7}(SrAl_2)_{0.3}O_{3.3-\delta}$	Method 2	4.23	13.21±0.01 (350–920 K) 24.68±0.06 (950–1230 K)	6.4±0.2
$(Sr_{0.95}Fe_{0.8}Al_{0.2})_{0.85}(SrAl_2)_{0.15}O_{3.02-\delta}$	Method 1	4.69	13.39±0.02 (350–920 K) 26.28±0.06 (920–1220 K)	6.3±0.2

oxygen permeability presented in this paper correspond to the membrane feed-side oxygen partial pressure (p_2) equal to 0.21 atm (atmospheric air); the thickness of the ceramic membranes (d) varied from 0.60 to 1.50 mm.

Results and discussion

Phase composition and microstructure

For both preparation routes, XRD analysis of $(SrFe)_{0.7}(SrAl_2)_{0.3}O_{3.3-\delta}$ ceramics confirmed the formation of dual-phase composites comprising a cubic perovskite-type solid solution and monoclinic $SrAl_2O_4$, as expected. No traces of phase impurities were detected. Figure 2 compares the room-temperature XRD patterns of the composites and parent phases. SEM inspections showed homogeneous composite microstructures, ensuring the percolation of major perovskite phase. Typical SEM micrographs are given in Fig. 3a,c; the perovskite grains are visible as light grey. The dissolution of iron in $SrAl_2O_4$ lattice evaluated by EDS was found negligible, in agreement with previous data [8]. At the same time, EDS results revealed that a significant part of $SrAl_2O_4$ is dissolved in the perovskite phase (Fig. 4). Similar conclusion was also drawn comparing the perovskite unit cell parameters in the composite materials with those in $Sr_{1-x}Fe_{1-y}Al_yO_{3-\delta}$ system [6]. The maximum concentration of aluminum cations in A-site stoichiometric $SrFe_{1-y}Al_yO_{3-\delta}$ is close to 35% [6], whereas, A-site deficiency of perovskite-type compounds may decrease their thermodynamic stability and, hence, solubility of dopants [18]. Furthermore, the ability of transition metal-containing perovskites to tolerate A-site vacancies is usually limited at 10–15% (e.g., [18] and references cited). Thus, the overall composition of the perovskite phase formed in $(SrFe)_{0.7}(SrAl_2)_{0.3}O_{3.3-\delta}$ composites should correspond to $Sr_{1-x}Fe_{1-2x}Al_{2x}O_{3-\delta}$ with x=0.08–0.15. Notice that, as transport properties of $SrFeO_3$-based solid solutions are superior compared to strontium aluminate [6, 8], the behavior of composite ceramics should be determined, in general, by the composition of perovskite grains and $SrAl_2O_4$ content.

One important observation made from the SEM/EDS data relates to significant microstructural differences between the materials prepared by methods 1 and 2, in spite of identical sintering conditions. The composite prepared by method 2 exhibits a larger size of the perovskite grains with essentially uniform distribution of Al^{3+} cations and a slightly lower content of separated $SrAl_2O_4$ (Figs. 3c and 4b); the composition of the perovskite phase was close to $Sr_{0.9}Fe_{0.8}Al_{0.2}O_{3-\delta}$. In the case of $(SrFe)_{0.7}(SrAl_2)_{0.3}O_{3.3-\delta}$ ceramics prepared by method 1, the perovskite grains are relatively small, and a substantial compositional gradient is observed; the Fe/Al cation ratio along grains of the perovskite phase varies in a

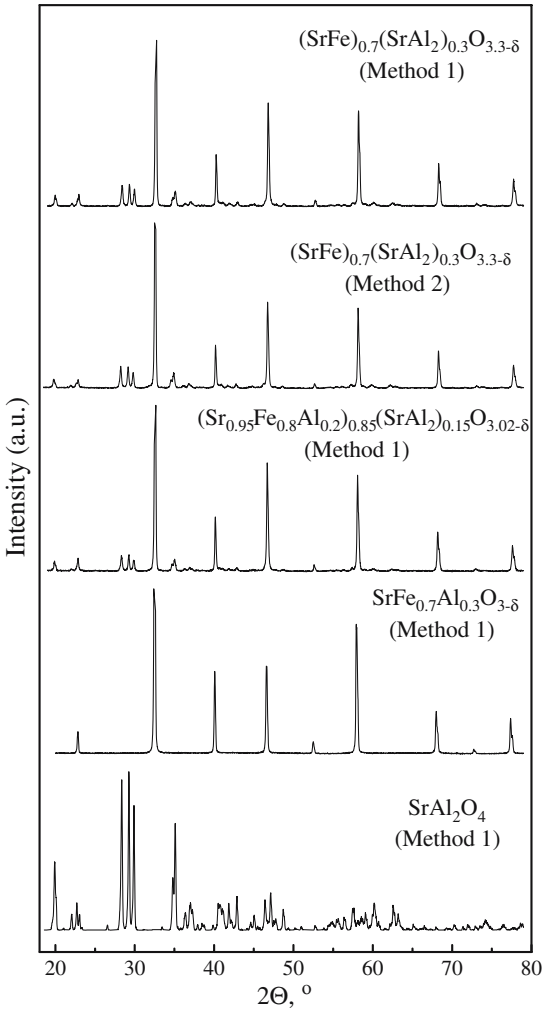

Fig. 2 XRD patterns of $(SrFe)_{0.7}(SrAl_2)_{0.3}O_{3.3-\delta}$ and $(Sr_{0.95}Fe_{0.8}Al_{0.2})_{0.85}(SrAl_2)_{0.15}O_{3.02-\delta}$ composite ceramics. The patterns of single-phase $SrFe_{0.7}Al_{0.3}O_{3-\delta}$ perovskite and $SrAl_2O_4$ [6, 8] are shown for comparison

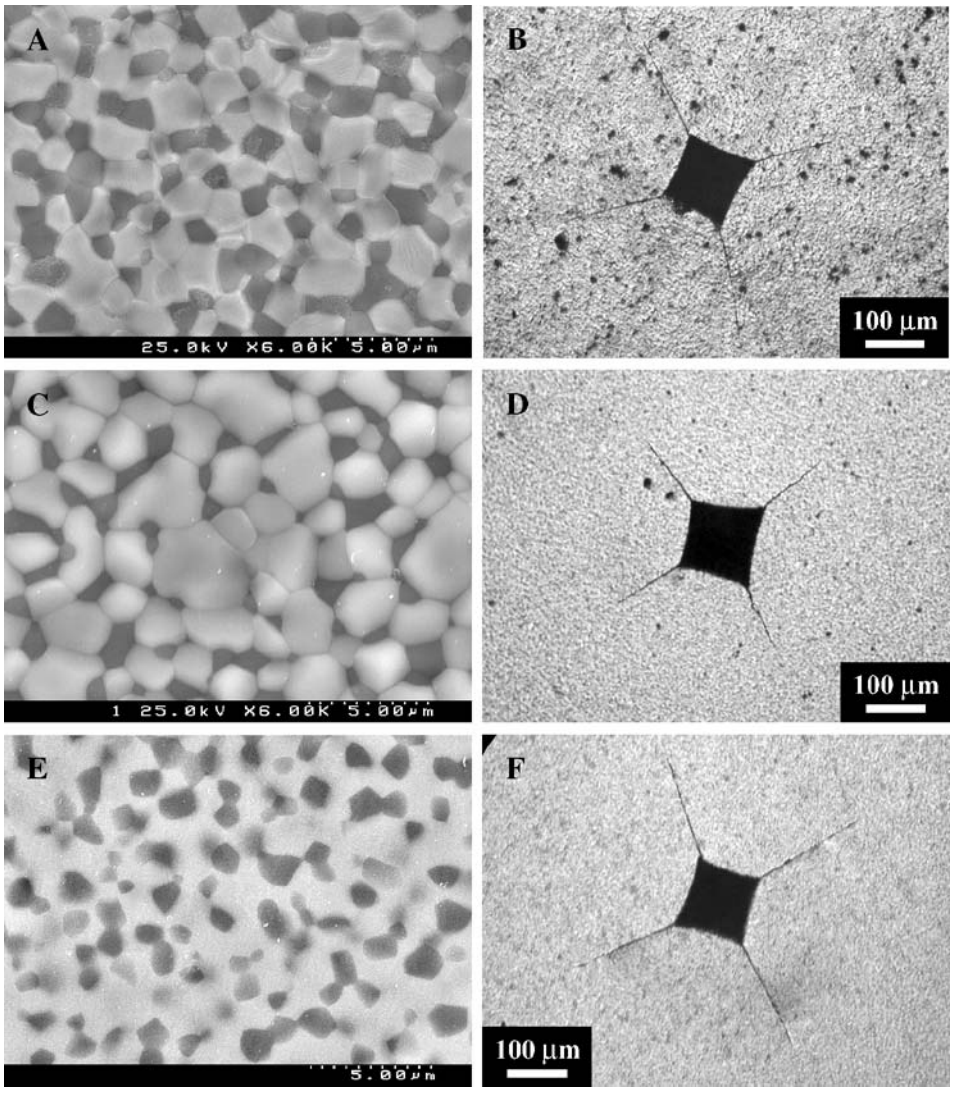

Fig. 3 SEM micrographs of polished and then thermally etched composite ceramics (**a**, **c**, **e**), and typical indents on the ceramics surface after Vickers hardness test (**b**, **d**, **f**): **a** and **b**—$(SrFe)_{0.7}(SrAl_2)_{0.3}O_{3.3-\delta}$ (method 1); **c** and **d**—$(SrFe)_{0.7}(SrAl_2)_{0.3}O_{3.3-\delta}$ (method 2), **e** and **f**—$(Sr_{0.95}Fe_{0.8}Al_{0.2})_{0.85}(SrAl_2)_{0.15}O_{3.02-\delta}$ (method 1). The *light* and *dark grains* correspond to $SrFeO_{3-\delta}$- and $SrAl_2O_4$-based phases, respectively

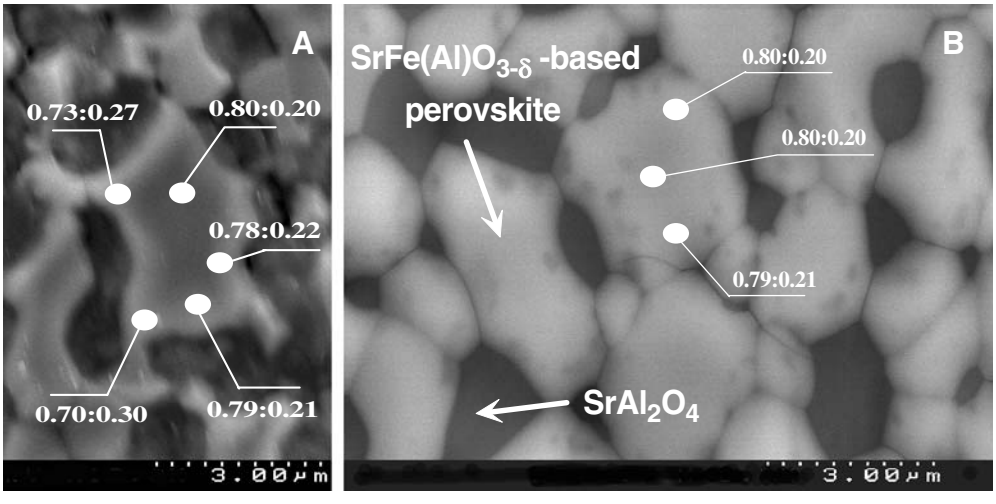

Fig. 4 Example of the local Fe: Al cation ratio in the perovskite grains of $(SrFe)_{0.7}(SrAl_2)_{0.3}O_{3.3-\delta}$ composites prepared by method 1 (**a**) and method 2 (**b**), estimated by EDS

wide range, from approximately 0.92:0.08 down to 0.70:0.30. Such inhomogeneities may be accompanied with a greater concentration of extended defects and catalytically active centers.

Thermomechanical properties and total conductivity

Despite the miscrostructural differences, Vickers hardness tests demonstrated essentially similar hardness of all composite ceramics studied in this work, within the limits of experimental error (Table 1). For all materials, the hardness is noticeably higher when compared to single-phase $SrFe_{0.7}Al_{0.3}O_{3-\delta}$ (Fig. 1). Also, the composites show relatively small cracks due to indentation (Fig. 3b,d), indicating a good fracture toughness.

Figure 5 presents the dilatometric curves of the title materials in air. At temperatures below 920 K, the average thermal expansion coefficients (TECs) decrease with increasing amount of $SrAl_2O_4$ phase (Table 1). Indeed, $SrAl_2O_4$ has moderate TEC values, $(9.5–9.8)\times10^{-6}$ K^{-1} at 350–1520 K, with a discontinuity due to phase transition into the hexagonal modification [8]; the thermal expansion of $SrFe_{0.7}Al_{0.3}O_{3-\delta}$ is considerably higher (Fig. 5). In the high-temperature range, the $(SrFe)_{0.7}(SrAl_2)_{0.3}O_{3.3-\delta}$ composite prepared by method 1 exhibits a slightly higher TEC compared to method 2. This may result, in particular, from a higher A-site deficiency of the perovskite phase near grain boundaries in the former case. Vacancies in a crystal lattice increase anharmonicity of atomic vibrations and may weaken metal–oxygen bonding [19, 20], thus leading to a greater expansion and, possibly, higher oxygen losses on heating. Similar effects are well-known for other ferrite-based mixed conductors, such as perovskite-type $Sr_{1-x}(Fe,Ti)O_{3-\delta}$ [21] and $(La_{0.5}Sr_{0.5})_{1-x}(Fe,Al)O_{3-\delta}$ [22].

The total conductivity of $(SrFe)_{0.7}(SrAl_2)_{0.3}O_{3.3-\delta}$ composites is predominantly p-type electronic in air, showing a pseudometallic behavior at temperatures above 950 K (Fig. 6). The latter trend, which is also typical for perovskite-like ferrites, originates from oxygen loss on heating accompanied with decreasing concentration of p-type charge carriers [4, 7, 21, 22]. As the properties of $SrAl_2O_4$ are rather insulating (inset in Fig. 6), the larger content of strontium aluminate phase leads to a moderately lower conductivity of $(SrFe)_{0.7}(SrAl_2)_{0.3}O_{3.3-\delta}$ prepared by method 1. In the case of method 1, the decrease in hole transport is also due to the aluminum enrichment of near-boundary layers of perovskite grains (Fig. 4a). For instance, the p-type electronic conductivity of Sr(Fe,Al)$O_{3-\delta}$ and $(La_{0.5}Sr_{0.5})_{1-x}(Fe,Al)O_{3-\delta}$ perovskites decreases on aluminum doping [6, 22].

Relationships between composite microstructure and ionic transport in $(SrFe)_{0.7}(SrAl_2)_{0.3}O_{3.3-\delta}$

Selected results on the oxygen permeation through dense $(SrFe)_{0.7}(SrAl_2)_{0.3}O_{3.3-\delta}$ membranes prepared by methods 1 and 2 are presented in Figs. 7 and 8, respectively. The values of specific oxygen permeability, $J(O_2)$, were calculated from the permeation flux density j as [6, 7, 15]:

$$J(O_2) = jd \cdot \left[\ln\frac{p_2}{p_1}\right]^{-1} \quad (1)$$

where p_1 is the oxygen partial pressure at the membrane permeate side, and d is the membrane thickness. The fluxes through $(SrFe)_{0.7}(SrAl_2)_{0.3}O_{3.3-\delta}$ composite ceramics made by method 1 decrease with increasing d, while the

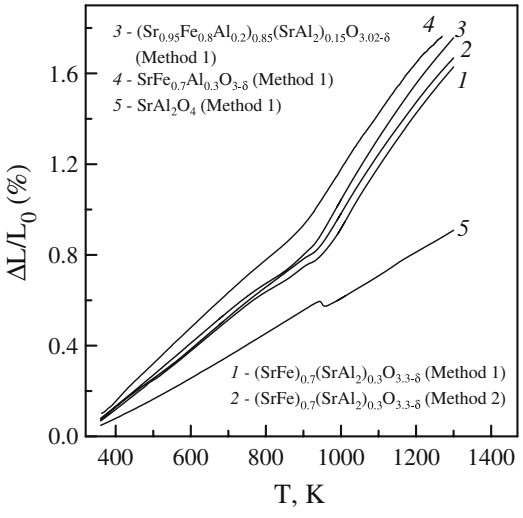

Fig. 5 Dilatometric curves of composite ceramics in air. Data on thermal expansion of $SrFe_{0.7}Al_{0.3}O_{3-\delta}$ and $SrAl_2O_4$ [6, 8] are shown for comparison

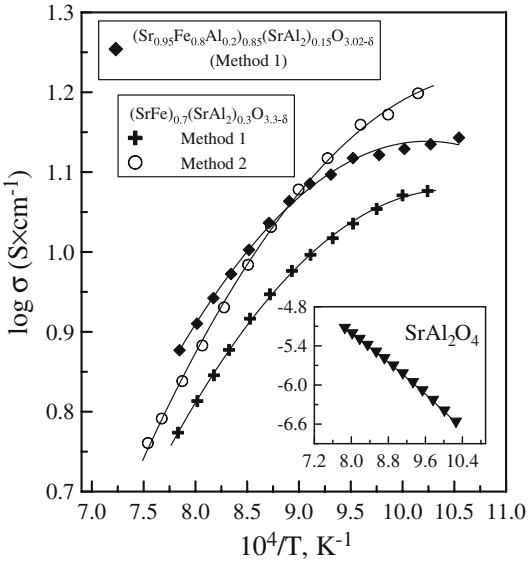

Fig. 6 Total conductivity of $(SrFe)_{0.7}(SrAl_2)_{0.3}O_{3.3-\delta}$ and $(Sr_{0.95}Fe_{0.8}Al_{0.2})_{0.85}(SrAl_2)_{0.15}O_{3.02-\delta}$ composites in air. Inset shows the conductivity of $SrAl_2O_4$ [8]

$J(O_2)$ values are almost thickness-independent within the limits of experimental uncertainty (Fig. 7). This behavior suggests that the overall oxygen transport is mainly governed by the bulk ambi-polar conduction [7]. Opposite trends are observed for the material obtained by method 2, where surface-exchange kinetics dominates at temperatures below 1123 K, vanishing when temperature increases.

The relative roles of the bulk ambipolar transport and surface exchange may be estimated decomposing the overall driving force, expressed as $\ln(p_2/p_1)$, into three contributions associated with membrane bulk and surfaces. The contributions to overcome limitations of surface exchange kinetics can be written as $\ln\left(p_2/p_2^{'}\right)$ for the feed side, with an oxygen partial pressure drop from p_2 to $p_2^{'}$, and $\ln\left(p_2^{'}/p_1\right)$ for the permeate side, with a drop from $p_1^{'}$ to p_1. The driving force to overcome the bulk resistance is, respectively, $\ln\left(p_2^{'}/p_1^{'}\right)$; the corresponding transport coefficient relates to the ambipolar conductivity $\sigma_{amb} = \sigma_o \times \sigma_e/(\sigma_o + \sigma_e)$, where σ_o and σ_e are the partial oxygen-ionic and electronic conductivities, correspondingly. The steady-state permeation flux may be expressed as $j = k_{ex}^{f} \ln\left(p_2/p_2^{'}\right) = k_{ex}^{p} \ln\left(p_1^{'}/p_1\right) = \left(RT/16F^2 d\right) \sigma_{amb} \times \ln\left(p_2^{'}/p_1^{'}\right)$, where k_{ex} is the exchange coefficient, and the superscripts f and p denote the feed- and permeate sides, respectively. This yields

$$\ln\left(\frac{p_2}{P_1}\right)\Big/ j = \left[\frac{16F^2}{RT\sigma_{amb}}\right] d + \left[k_{ex}^{f}\right]^{-1} + \left[k_{ex}^{p}\right]^{-1} = \left[\frac{16F^2}{RT\sigma_{amb}}\right] \times (d + d_c), \quad (2)$$

where the critical thickness d_c corresponds to the transition from exchange control, for thin samples, to bulk transport control, for thicker samples. Eq. 2 was used to extract the estimates of ambipolar conductivity (Fig. 9a) and surface exchange coefficients (Fig. 9b) from the data shown in Figs. 7 and 8. The ambipolar conductivity of $(SrFe)_{0.7}(SrAl_2)_{0.3}O_{3.3-\delta}$ composites is essentially independent of the preparation technique. In fact, although the values of σ_{amb} are slightly lower for the material prepared by method 2 at oxygen chemical potentials close to atmospheric, this effect is comparable to the experimental error and decreases on reduction. One possible reason is the lower concentration of Al^{3+} in the near-boundary layers of perovskite grains, which may lead to lower oxygen-vacancy concentration and, therefore, ionic conduction.

On the contrary, the microstructural differences have a dramatic influence on the surface exchange kinetics. At 1223 K, the composite prepared by method 1 shows approximately eight times faster oxygen exchange compared to method 2 (Fig. 9b). As evidenced by data on

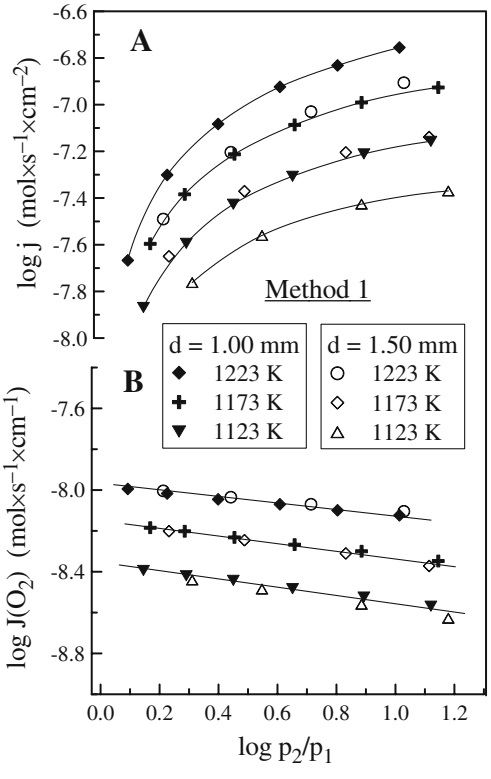

Fig. 7 Oxygen permeation fluxes (**a**) and specific oxygen permeability (**b**) of $(SrFe)_{0.7}(SrAl_2)_{0.3}O_{3.3-\delta}$ composite membranes prepared by method 1

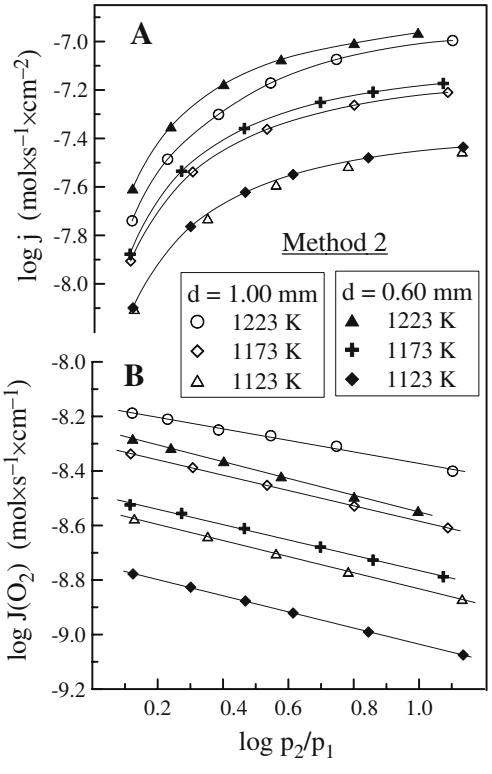

Fig. 8 Oxygen permeation fluxes (**a**) and specific oxygen permeability (**b**) of $(SrFe)_{0.7}(SrAl_2)_{0.3}O_{3.3-\delta}$ membranes prepared by method 2

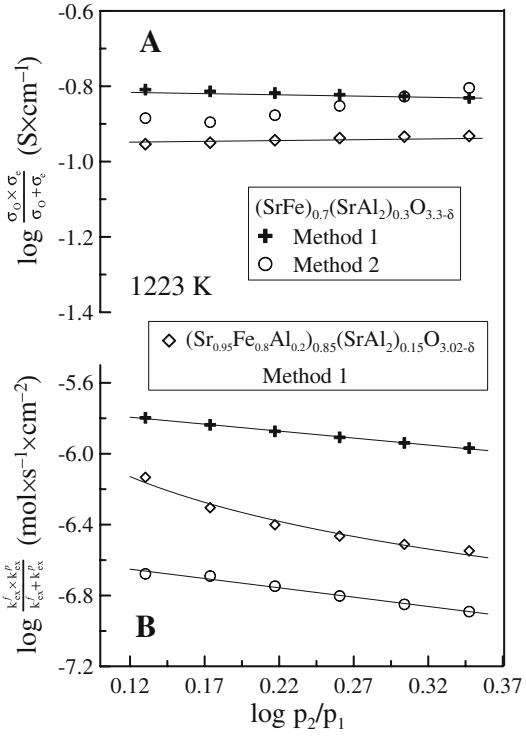

Fig. 9 Dependencies of the average ambipolar conductivity (**a**) and oxygen exchange coefficients (**b**) of composite ceramics on the oxygen partial pressure gradient at 1,223 K

oxygen permeation (Figs. 7 and 8), decreasing temperature leads even to a greater difference. Most likely, this behavior is caused by significant compositional inhomogeneities in the perovskite grains and higher concentration of grain boundaries and/or extended defects in the material obtained by method 1. Such defects may increase the concentration of weakly bonded oxygen states and form catalytically active centers participating in oxygen exchange at the membrane surface [23, 24]. Analogous tendencies were observed earlier for the GNP-synthesized $LaGa_{0.65}Ni_{0.20}Mg_{0.15}O_{3-\delta}$ [14] and $La_2Ni_{0.9}Co_{0.1}O_{4+\delta}$ [24], where locally inhomogeneous microstructure facilitates the surface processes.

To verify this conclusion, one $(SrFe)_{0.7}(SrAl_2)_{0.3}O_{3.3-\delta}$ membrane prepared by method 2 was activated applying porous layers of the same composition onto both surfaces. The layers with sheet density (d_s) of approximately 7 mg/cm^2 were sintered at 1373 K for 2 h, impregnated with a Pr-containing solution, dried and finally annealed at 1440 K. The loading density of praseodymium oxide was approximately 4 mg/cm^2. Typical SEM micrographs of surface-modified membrane are given in Fig. 10a,b. Figures 11 and 12 compare oxygen fluxes through the composite membranes with and without surface modification. The activation leads to a significant increase in the specific oxygen permeability and decreases the corresponding activation energy. For the surface-modified membrane obtained by method 2, the values of $J(O_2)$ became similar to those of the composite prepared by method 1.

Properties of $(Sr_{0.95}Fe_{0.8}Al_{0.2})_{0.85}(SrAl_2)_{0.15}O_{3.02-\delta}$ composite

The variations in properties of $(SrFe)_{0.7}(SrAl_2)_{0.3}O_{3.3-\delta}$ materials prepared by the different routes are associated with changes in the constituents phase ratio, compensated by changing the overall Al^{3+} concentration and A-site deficiency of the perovskite component. The latter factor seems to limit $SrAl_2O_4$ dissolution in $Sr_{1-x}(Fe,Al)O_{3-\delta}$ lattice. To assess the effects of phase ratio, dense $(Sr_{0.95}Fe_{0.8}Al_{0.2})_{0.85}(SrAl_2)_{0.15}O_{3.02-\delta}$ ceramics were prepared by method 1 using the same sintering conditions. In this case, composition of the perovskite grains may vary in a relatively narrow range between $Sr_{0.95}Fe_{0.8}Al_{0.2}O_{3-\delta}$ and $Sr_{0.90}Fe_{0.7}Al_{0.3}O_{3-\delta}$, while the amount of $SrAl_2O_4$ phase is significantly smaller if compared to $(SrFe)_{0.7}(SrAl_2)_{0.3}O_{3.3-\delta}$ obtained by method 1 (Fig. 3e). As expected, this results in higher thermal expansion and total conductivity (Figs. 5 and 6). The microhardness and fracture toughness of $(Sr_{0.95}Fe_{0.8}Al_{0.2})_{0.85}(SrAl_2)_{0.15}O_{3.02-\delta}$ are close to the properties of other composites studied (Table 1).

The membrane thickness dependencies of the oxygen permeability of $(Sr_{0.95}Fe_{0.8}Al_{0.2})_{0.85}(SrAl_2)_{0.15}O_{3.02-\delta}$ (Fig. 13) indicate that the overall oxygen transport is determined by both bulk ambi-polar diffusion and surface exchange kinetics, making it possible to evaluate these factors by Eq. 2. The higher Al^{3+} content in the perovskite grains of $(Sr_{0.95}Fe_{0.8}Al_{0.3})_{0.85}(SrAl_2)_{0.15}O_{3.02-\delta}$, at least with respect to $(SrFe)_{0.7}(SrAl_2)_{0.3}O_{3.3-\delta}$ ceramics prepared by method 2, results in a lower ambi-polar conductivity (Fig. 9). At the same time, the exchange reaction of the former material is faster. Comparing the corresponding microstructures, one may select two factors affecting the kinetics of interfacial oxygen exchange in $Sr_{1-x}(Fe,Al)O_{3-\delta} - SrAl_2O_4$ composites, namely, the surface concentration of grain boundaries and the Al:Fe cation ratio in the perovskite grains. The content of $SrAl_2O_4$ also seems to play a positive role, mainly suppressing perovskite grain growth and, thus, enlarging the grain boundary area.

Behavior under air/(H_2–H_2O) gradients

The permeation-limiting effects of exchange-related processes are expected to increase dramatically under high $p(O_2)$ gradients, when one side of the membrane is exposed to a reducing atmosphere [6, 24, 25]. In these conditions, however, the surface exchange limitations may enhance the membrane stability, preventing bulk reduction of mixed conducting ceramics [25–27]. Namely, when the permeation is controlled by surface-related processes, such as recombination of lattice O^{2-} anions, stagnated gas diffusion or oxidation reactions at the gas/solid interface, the oxygen chemical potential on the outermost layer of the mixed conducting material should always be higher than that in the gas environment. Selected results of testing $Sr_{1-x}(Fe,Al)O_{3-\delta} - SrAl_2O_4$ composite membranes

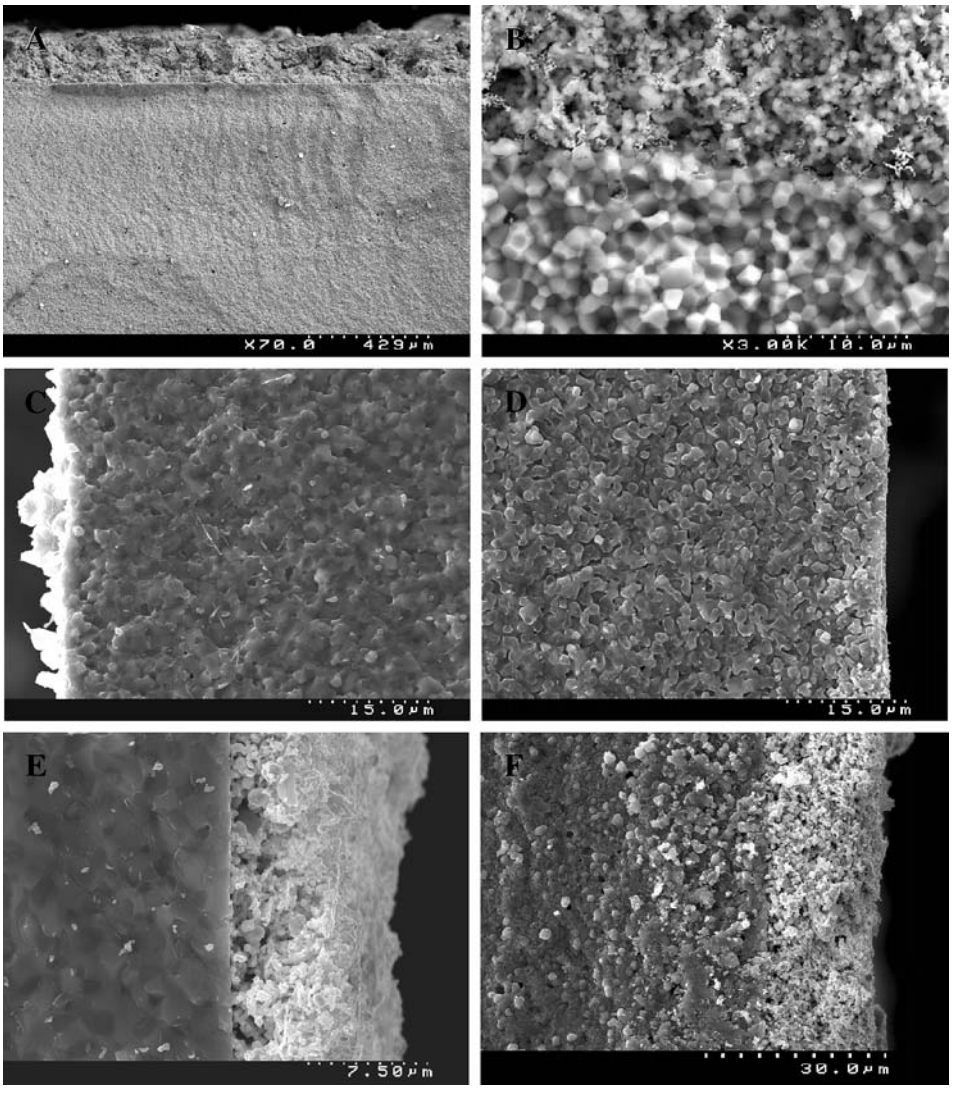

Fig. 10 SEM micrographs of the surface-activated $(SrFe)_{0.7}(SrAl_2)_{0.3}O_{3.3-\delta}$ membrane prepared by method 2 (**a** and **b**); fractured cross-section of $(Sr_{0.95}Fe_{0.8}Al_{0.2})_{0.85}(SrAl_2)_{0.15}O_{3.02-\delta}$ membrane near the feed- (**c**) and permeate side (**d**) after the oxygen permeation measurement under air/(H_2–H_2O–N_2) gradients at 1023–1073 K for 1,600 h; as-prepared $(SrFe)_{0.7}(SrAl_2)_{0.3}O_{3.3-\delta}$ membrane (method 1) with porous CGO/Pt layer (**e**); fractured cross-section of $(SrFe)_{0.7}(SrAl_2)_{0.3}O_{3.3-\delta}$ membrane (method 1) with CGO/Pt layer after testing under air/10%H_2–90%N_2 gradient at 1073 K for 270 h (**f**)

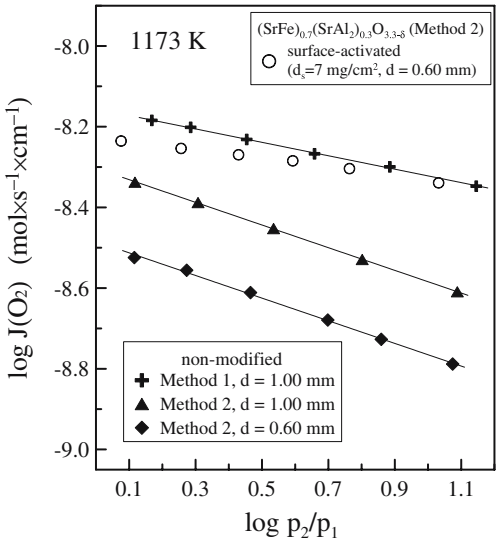

Fig. 11 Specific oxygen permeability $(SrFe)_{0.7}(SrAl_2)_{0.3}O_{3.3-\delta}$ membranes with and without surface modification (see text)

under air/(H_2–H_2O)–N_2 gradients, used to model the behavior in strongly reducing gas mixtures formed due to methane oxidation, are presented in Figs. 14 and 15.

In contrast to other membrane systems [24, 25], no direct correlation between the hydrogen partial pressure and oxygen flux across the membrane was observed, whereas, the permeation rate increases with increasing hydrogen flux supplied onto the membrane. This shows that the H_2 oxidation kinetics is not the only permeation-determining factor. Such behavior may be due to mass transfer-limiting effects in the near-surface gas layer, associated with a significant difference of the oxygen chemical potentials at the ceramic surface and in the gas phase, and/or to the surface decomposition and microstructural reconstruction of the membranes. In the case of mass-transfer limitations, increasing hydrogen flux should accelerate the displacement of oxidized species (H_2O) with unreacted H_2, thus decreasing $p(O_2)$ at the membrane surface. A higher oxygen chemical potential gradient across the membrane increases the permeation flux and hydrogen conversion until a critical value of the inlet H_2 flux is reached; then the

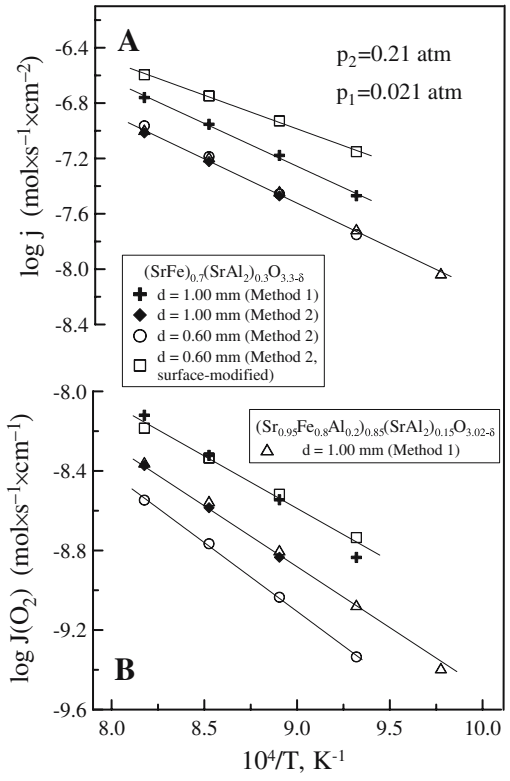

Fig. 12 Temperature dependence of the oxygen permeation fluxes (**a**) and specific oxygen permeability (**b**) through surface-activated and non-modified composite membranes under fixed oxygen partial pressure gradient

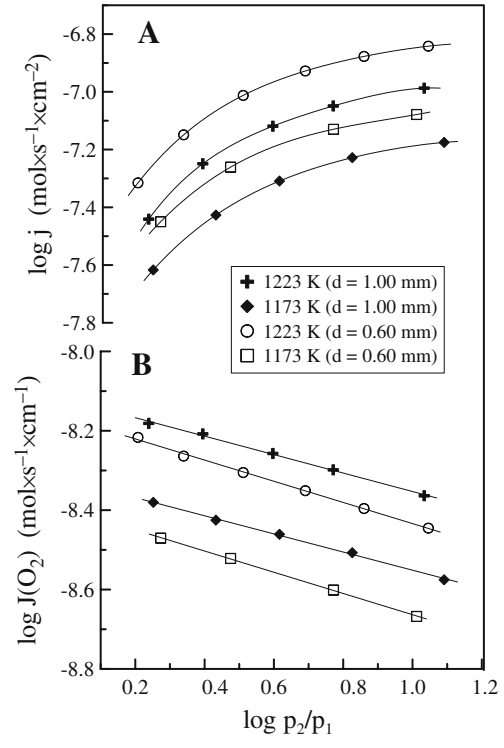

Fig. 13 Oxygen permeation fluxes (**a**) and specific oxygen permeability (**b**) of $(Sr_{0.95}Fe_{0.8}Al_{0.2})_{0.85}(SrAl_2)_{0.15}O_{3.02-\delta}$ composite membranes prepared by method 1

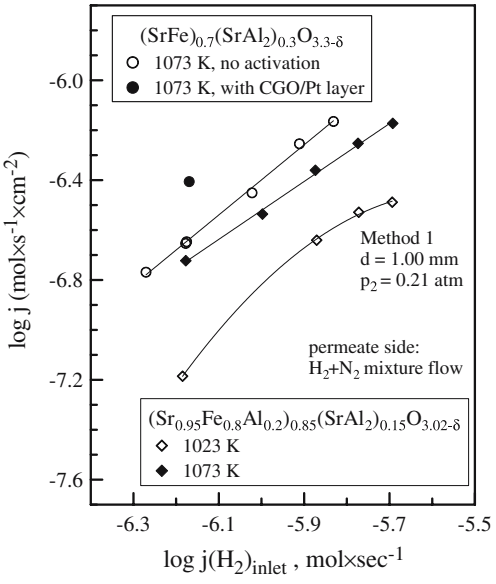

Fig. 14 Oxygen permeation fluxes through the composite membranes prepared by method 1 under air/(H_2–H_2O)–N_2 gradient vs hydrogen flux supplied onto the membrane permeate side. The permeation flux for $(SrFe)_{0.7}(SrAl_2)_{0.3}O_{3.3-\delta}$ membrane with CGO/Pt layer is given for the initial period of time. The oxygen partial pressure at the permeate side (p_1) varied in the range 5×10^{-22} to 4×10^{-19} atm

permeation should be limited exclusively by the hydrogen oxidation rate, with $j(H_2)$-independent oxygen fluxes and a decrease in the hydrogen conversion rate when the inlet H_2 flux increases.

The limiting role of gas-phase mass transport should become more pronounced in the case of gas diffusion in the pores or microcracks of a partly decomposed layer of the membrane surface. In the case of $Sr_{1-x}(Fe,Al)O_{3-\delta}$ –

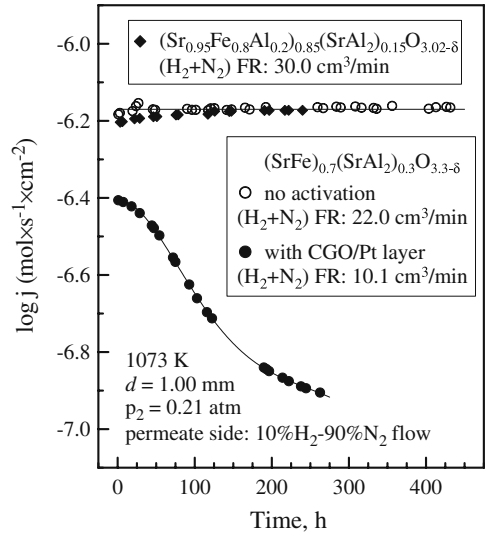

Fig. 15 Time dependence of the oxygen permeation fluxes through composite membranes prepared by method 1 at 1073 K and different flow rates (FR) of 10%H_2–90%N_2 mixture. The oxygen partial pressure at the permeate-side (p_1) varied in the range 2×10^{-20} to 2×10^{-18} atm

Fig. 16 Dense $(SrFe)_{0,7}(SrAl_2)_{0.3}O_{3.3-\delta}$ membranes fabricated from the powder synthesized by method 2. Insets illustrate surface morphology of the membranes

$SrAl_2O_4$ composites, partial reduction of the membrane surface exposed to H_2-containing atmospheres is very likely as the oxygen partial pressure in the outlet gas mixture stands below the low-$p(O_2)$ stability boundary of the $SrFe(Al)O_{3-\delta}$ perovskites under equilibrium conditions [6]. No traces of surface reduction were, however, revealed by the SEM/EDS analysis, in spite of minor microstructural reconstruction caused by the kinetic demixing phenomena [2, 6, 25]. As an illustration, Fig. 10 shows the cross-sections of one $(Sr_{0.95}Fe_{0.8}Al_{0.2})_{0.85}(SrAl_2)_{0.15}O_{3.02-\delta}$ membrane near the feed (C) and permeate (D) side surfaces. This membrane was tested under air/$(H_2$–$H_2O)$–N_2 gradients at 1023–1073 K for 1,600 h without failure. Note that the oxygen permeation fluxes through composite ceramics are essentially time-independent (Fig. 15). The stable operation of $SrFe(Al)O_{3-\delta} - SrAl_2O_4$ composite membranes under high-oxygen chemical potential gradients is only possible due to kinetic factors resulting from surface-limited oxygen transport, as for single-phase $SrFe_{0.7}Al_{0.3}O_{3-\delta}$ [6].

These statements were validated applying a porous catalytically active layer onto the permeate-side surface of $(SrFe)_{0.7}(SrAl_2)_{0.3}O_{3.3-\delta}$ membrane prepared by method 1. The layer (Fig. 10e), consisting of $Ce_{0.8}Gd_{0.2}O_{2-\delta}$ (CGO) and metallic Pt (50:50 wt%), with the sheet density of 8.1 mg/cm^2, was sintered at 1373 K for 1 h. Although the rate of 10%H_2–90%N_2 mixture supplied onto activated membrane was lower than in other cases (Fig. 15), this membrane showed a substantial degradation with time and deep microstructural changes (Fig. 10f). Thus, as expected from the kinetic stabilization models [26, 27], surface activation may promote the exchange and oxidation reactions, but simultaneously leads to decreasing oxygen chemical potential difference between the membrane surface and gas phase. The latter effect promotes a deep membrane decomposition with subsequent pore propagation to the bulk, accelerating further reduction.

Tubular membranes

The results show that $SrFe(Al)O_{3-\delta} - SrAl_2O_4$ composite membranes prepared via different processing routes have similar mechanical properties and substantially high oxygen permeability, but the surface exchange processes are strongly dependent on the microstructural factors. Also, excessive enhancement of the exchange kinetics due to deposition of catalytically active layers may have a global negative impact. As $(SrFe)_{0.7}(SrAl_2)_{0.3}O_{3.3-\delta}$ synthesized by combustion spray pyrolysis (method 2) exhibits relatively high ionic conductivity and moderately slow exchange, this composite was considered as a candidate material for the electrochemical membrane reactors. The tubular membranes were surface-modified by mechanical treatment without incorporation of catalytically active components, which may shift oxygen chemical potential at the membrane surface below the thermodynamic stability limit.

The dense tubes of $(SrFe)_{0.7}(SrAl_2)_{0.3}O_{3.3-\delta}$ composite were fabricated by the cold isostatic pressing (CIP) using a Burton Corblin instrument (France), with pressure vessel of 100 mm in diameter and 500 mm in length. In the course of processing, the ball-milled powder was filled around a steel mandrel with 6.35 mm diameter positioned in the center of a flexible latex hose. Special care was taken to distribute the powder symmetrically around the mandrel, aiming at minimizing the variations of circular wall thickness and the eccentricity of tube opening with respect to outer diameter of the tube; sticking of the latex hose to the green compact was avoided to obtain crack-free tube walls. After isostatic compaction at 175 MPa, the green tubes were pre-sintered in air at 1273 K for 1 h. Then the outer surface area of the tubular membranes was enlarged by mechanical scratching with a hardened steel saw blade in longitudinal direction. After such treatment, tubular membranes with 30–40 cm length, 5 mm inner diameter and 1 mm average wall thickness (Fig. 16) were sintered at 1623 K for 5 h. Testing of the tubes under the total pressure gradient of 2–3 atm at room temperature confirmed gas-tightness; analogous results were obtained at 973–1173 K when the leakage of atmospheric air in a helium flow, passed inside the membranes, was lower than the detection limit of gas-chromatographic analysis.

Acknowledgements This work was partially supported by the FCT, Portugal (projects POCI/CTM/58570/2004, SFRH/BPD/15003/2004 and SFRH/BPD/11606/2002), and by the NATO Science for Peace program (project 978002). Experimental assistance of A. Shaula and I. Marozau is gratefully acknowledged.

References

1. Dyer PN, Richards RE, Russek SL, Taylor DM (2000) Solid State Ionics 134:21
2. Diethelm S, Sfeir J, Clemens F, Van herle J, Favrat D (2004) J Solid State Electrochem 8:611
3. Pei S, Kleefisch MS, Kobylinski TP, Faber J, Udovich CA, Zhang-McCoy V, Dabrowski B, Balachandran U, Mieville RL, Poeppel RB (1995) Catal Letters 30:201
4. Bahteeva JA, Leonidov IA, Patrakeev MV, Mitberg EB, Kozhevnikov VL, Poeppelmeier KR (2004) J Solid State Electrochem 8:578
5. Mazanec TJ, Cable TL, Frye JG, Kliewer WR (1997) US Patent 5591315
6. Kharton VV, Shaula AL, Snijkers FMM, Cooymans JFC, Luyten JJ, Yaremchenko AA, Valente AA, Tsipis EV, Frade JR, Marques FMB, Rocha J (2005) J Membr Sci 252:215
7. Kharton VV, Yaremchenko AA, Shaula AL, Viskup AP, Marques FMB, Frade JR, Naumovich EN, Casanova JR, Marozau IP (2004) Defect Diffus Forum 226–228:141
8. Yaremchenko AA, Kharton VV, Valente AA, Shaula AL, Marques FMB, Rocha J (2005) Solid State Ionics (in press)
9. Christie GM, van Berkel FPF (1996) Solid State Ionics 83:17
10. Kharton VV, Marques FMB (2002) Curr Opin Solid State Mater Sci 6:261
11. Zhang K, Yang YL, Ponnusamy D, Jacobson AJ, Salama K (1999) J Mater Sci 34:1367
12. Kharton VV, Naumovich EN, Kovalevsky AV, Viskup AP, Figueiredo FM, Bashmakov IA Marques FMB (2000) Solid State Ionics 138–135
13. Diethelm S, Van herle J, Sfeir J, Buffat P (2005) J Eur Ceram Soc 25:2191
14. Shaula AL, Viskup AP, Kharton VV, Logvinovich DI, Naumovich EN, Frade JR, Marques FMB (2003) Mater Res Bull 38:353
15. Kharton VV, Kovalevsky AV, Yaremchenko AA, Figueiredo FM, Naumovich EN, Shaula AL, Marques FMB (2002) J Membr Sci 195:277
16. Steele BCH (1995) Solid State Ionics 75:157
17. Murphy MW, Armstrong TR, Smith PA (1997) J Am Ceram Soc 80:165
18. Kharton VV, Yaremchenko AA, Naumovich EN (1999) J Solid State Electrochem 3:303
19. West AR (1984) Solid state chemistry and its applications. Wiley, Chichester NY Brisbane
20. Hayashi H, Kanoh M, Quan CJ, Inaba H, Wang S, Dokiya M, Tagawa H (2000) Solid State Ionics 132:227
21. Kharton VV, Kovalevsky AV, Tsipis EV, Viskup AP, Naumovich EN, Jurado JR, Frade JR (2002) J Solid State Electrochem 7:30
22. Kharton VV, Waerenborgh JC, Viskup AP, Yakovlev SO, Patrakeev MV, Gaczyñski P, Marozau IP, Yaremchenko AA, Shaula AL, Samakhval VV (2006) J Solid State Chem (in press)
23. Isupova LA, Yakovleva IS, Rogov VA, Alikina GM, Sadykov VA (2004) Kinet Catal 45:446
24. Kharton VV, Yaremchenko AA, Tsipis EV, Valente AA, Patrakeev MV, Shaula AL, Frade JR, Rocha J (2004) Appl Catal A 261:25
25. Bouwmeester HJM, Burggraaf AJ (1996) Dense ceramic membranes for oxygen separation. In: Burggraaf AJ, Cot L (eds) Fundamentals of inorganic membrane science and technology. Elsevier, Amsterdam, pp 435–528
26. Hendriksen PV, Larsen PH, Mogensen M, Poulsen FW, Wiik K (2000) Catal Today 56:283
27. Kharton VV, Yaremchenko AA, Valente AA, Sobyanin VA, Belyaev VD, Semin GL, Veniaminov SA, Tsipis EV, Shaula AL, Frade JR, Rocha J (2005) Solid State Ionics 176:781